Full Text View

Volume 29, Issue 3 (March 1999)

Journal of Physical Oceanography
Article: pp. 519–529 | Abstract | PDF (159K)

Universality of the Modeled Small-Scale Response of the Upper Tropical Ocean to Squall Wind Forcing

R. A. Richardson, G. G. Sutyrin, D. Hebert, and L. M. Rothstein

Graduate School of Oceanography, University of Rhode Island, Narragansett, Rhode Island

(Manuscript received February 3, 1997, in final form January 29, 1998)

DOI: 10.1175/1520-0485(1999)029<0519:UOTMSS>2.0.CO;2

ABSTRACT

The upper ocean response to idealized surface wind forcing that is representative of conditions observed during the TOGA-COARE Intensive Observation Period is studied by numerical simulations using a second-moment closure model. A set of experiments is described with a variety of squall-like wind stress distributions and linear initial stratification in the ocean. Several physical regimes of turbulent mixing and decay during and after wind forcing are described. Differences in the structure of the upper and lower parts of the mixing layer are analyzed. The results indicate an exponential decay of turbulent kinetic energy (TKE) with time after surface forcing is removed, and TKE source terms continue to play an important role.

The velocity and density structure after the squall are found to be universal, with a nearly constant Richardson number throughout the mixing layer. It is demonstrated that this implies that the mixed layer depth is determined by the initial buoyancy frequency and total momentum input from the wind stress in the same manner as in the bulk mixed layer models. It does not depend essentially on the squall duration or the time evolution of the wind stress during the squall.

1. Introduction

Squalls are a ubiquitous source of very strong winds in the COARE domain (Webster and Lukas 1992) and mechanically drive strong mixing in the upper ocean. However, the large rainfall associated with these squalls tends to suppress the wind-induced mixing. Although these squalls are intense meteorological features, they are small (horizontal scales of several kilometers) and short-lived (lifetimes of several hours). Thus, it is not known whether they have a profound net effect on the mixed layer dynamics. Since mixing is an irreversible process, it is important

to understand the influence of squalls on the mixed layer dynamics of the warm pool.

There have been numerous studies that have attempted to simulate the oceanic mixed layer response to atmospheric forcing. In general, three different modeling approaches have been employed: 1) bulk models, in which the integrated properties over the entire mixed layer are considered, assuming temperature and velocity profiles a priori (e.g., Kraus and Turner 1967; Pollard et al. 1973; Niiler and Kraus 1977; Kraus 1988); 2) eddy coefficient models, in which turbulence terms such as Reynolds stresses are parameterized via eddy diffusivity coefficients that are generally variable in space and time and are calculated using some sort of turbulence closure scheme (e.g., Munk and Anderson 1948;Mellor and Durbin 1975; Kundu 1980; Klein and Coantic 1981; Andre and Lacarrere 1985; Martin 1985); and 3) combinations of the previous two (e.g., Price et al. 1986; Chen et al. 1994). However, the main purpose of these studies has been to examine the deepening of the mixed layer resulting from increases in wind stress or surface cooling without consideration of the decay of turbulence after the surface forcing is shut off.

The decay of turbulence in the absence of sources has been a central topic in turbulence research for many decades. For isotropic turbulence in homogeneous fluids, the classical result from laboratory tests is that the turbulence kinetic energy decays as t^{-1} and the turbulence energy dissipation rate decays as t^{-2} (Batchelor and Townsend 1948). Much less is known about decaying turbulence in a stably stratified ocean, where the stratification (N^{-1}, where N is the buoyancy frequency) provides a natural timescale. While Caldwell (1983) and Gregg (1987) have argued that, in the absence of an energy source, decay times are comparable to N^{-1}, others (e.g. Gibson 1982) have presented the case for long-lived source-free turbulence. Dillon (1982), Crawford (1986), and Moum (1996) have employed different approaches to arrive at a common conclusion: the timescale for viscous dissipation of stratified turbulence is significantly less than N^{-1}.

The decay of oceanic turbulence after a wind forcing event has been the subject of recent observational work (Smyth et al. 1996). In particular, the authors note that their microstructure observations of the decay of turbulence after a squall reveal an exponential decay of TKE with time. Furthermore, they argue that this decay is slower than would be expected if the TKE dissipation term were the only important contributor in the total evolution of the TKE. This leads them to conclude that TKE source terms remain important, even after the effects of surface wind forcing have been dramatically reduced by the presence of a stable freshwater cap at the ocean surface.

In the present work we want to identify the main regimes of wind induced mixing and subsequent turbulence decay in a simple scenario without surface heating/cooling or rainfall. Here the removal of the effects of wind forcing is simply accomplished by turning off the wind.

We use a one-dimensional second-moment closure model to study the upper-ocean response to idealized surface forcing representative of conditions observed during the TOGA COARE Intensive Observation Period. We focus on one-dimensional processes because the short timescale of the forcing and the near-equatorial regime make a number of three-dimensional processes, such as inertial oscillations, less relevant here than they would be in a midlatitude context [e.g., the Ocean Storms experiment (D'Asaro 1985)]. Second-moment closure models remain among the most computationally efficient and accurate tools for practical applications. The Mellor–Yamada level 2.5 turbulence closure model (MY2.5) that we employ is based on prognostic equations for turbulence energy and macroscale and has been widely used for a range geophysical studies.

2. Mathematical formulation

a. Basic equations

We use a one-dimensional version of the MY2.5 model, that is, horizontal variations are neglected and therefore the mean vertical velocity is zero. The equations for the ensemble-mean horizontal velocity $\mathbf{V} = (V_x, V_y)$, potential temperature Θ, salinity S, and turbulent kinetic energy $E = \langle u^2 + v^2 + w^2 \rangle/2$ can be written as

$$\frac{\partial E}{\partial t} = -\frac{\partial F}{\partial z} + P_s + P_b - \epsilon. \qquad (4)$$

Here we use the Cartesian coordinate system with the z axis directed downward from the sea surface and f is the Coriolis frequency. Uppercase letters represent ensemble mean variables, while lowercase letters are the fluctuating, turbulent variables. Angle brackets represent ensemble means of turbulent variables. It should perhaps be noted that the model does not solve for w explicitly, but rather solves for the angle-bracketed turbulent flux terms, in which w is implicit. Besides the turbulence kinetic energy dissipation rate ϵ, the terms on the rhs of (4) are:the vertical flux of turbulent energy

$$F = \left\langle w\left(\frac{p}{\rho_0} + \frac{u^2 + v^2 + w^2}{2}\right)\right\rangle, \qquad (5)$$

the production by mean velocity shear

$$P_s = -\langle w\mathbf{v}\rangle\frac{\partial \mathbf{V}}{\partial z}, \qquad (6)$$

and the decay or production by buoyancy flux

$$P_b = -\frac{g}{\rho_0}\langle w\rho\rangle = g\alpha_\theta\langle w\theta\rangle - g\beta\langle ws\rangle, \qquad (7)$$

which is computed according to a linearized equation of state. The coefficients α_θ and β are assumed to be constants typical of the upper tropical ocean, g is the gravitational acceleration, and ρ_0 is the reference density.

In the Mellor–Yamada level 2.5 turbulence closure model, the vertical fluxes are given by

$$\langle w\mathbf{v}\rangle = -qlS_H\frac{\partial \mathbf{V}}{\partial z}, \qquad P_b = qlS_HN^2,$$

$$F = -qlS_q\frac{\partial E}{\partial z}, \qquad (8)$$

where $q = (2E)^{1/2}$ is the rms velocity of turbulence and N is the buoyancy frequency,

$$N^2 = g\left(-\alpha_\theta\frac{\partial \theta}{\partial z} + \beta\frac{\partial S}{\partial z}\right). \qquad (9)$$

The turbulence macroscale l is introduced according to the Kolmogorov hypothesis of local, small-scale isotropy

$$l = \frac{q^3}{B_1\epsilon}, \qquad (10)$$

while the stability function S_H and the turbulent Prandtl number σ are related to the parameters

$$G_M = \frac{l^2}{q^2}\left(\frac{\partial \mathbf{V}}{\partial z}\right)^2, \qquad G_H = \frac{l^2N^2}{q^2} \qquad (11)$$

by the following algebra:

$$= A_2 \tag{12}$$

$$S_H[12A_1^2G_H + 9A_1A_2G_H + \sigma(1 + 6A_1^2G_M + 9A_1A_2G_H)]$$
$$= A_1(1 - 3C_1), \tag{13}$$

with the empirical constants $(A_1, A_2, B_1, B_2, C_1) = (0.92, 0.74, 16.6, 10.1, 0.08)$ (Mellor and Yamada 1982) determined from laboratory data.

It is useful to express S_H and σ in terms of the ratio of production to dissipation rates $(P_s + P_b)/\epsilon$ and the flux Richardson number R_f:

$$S_H(\sigma G_M - G_H) = \frac{P_s + P_b}{B_1\epsilon}, \qquad \frac{G_H}{\sigma G_M} = R_f, \tag{14}$$

so that, from Eqs. (12)–(13)

$$S_H = A_2\frac{\alpha_1 - \alpha_2 R_f}{1 - R_f},$$

$$\sigma = \frac{A_1}{A_2}\frac{\alpha_1 - 3C_1 - \alpha_3 R_f}{\alpha_1 - \alpha_4 R_f}, \tag{15}$$

where the coefficients α_i linearly depend on $(P_s + P_b)/\epsilon$ as

$$\alpha_1 \equiv 1 - \frac{6A_1}{B_1}\frac{P_s + P_b}{\epsilon} = 1 - 0.33\frac{P_s + P_b}{\epsilon}, \tag{16}$$

$$\alpha_2 \equiv 1 + \frac{12A_1 + 3B_2}{B_1}\frac{P_s + P_b}{\epsilon}$$
$$= 1 + 2.5\frac{P_s + P_b}{\epsilon}, \tag{17}$$

$$\alpha_3 \equiv \alpha_1 - 3C_1 + \frac{18A_1 + 9A_2}{B_1}\frac{P_s + P_b}{\epsilon}$$
$$= 0.76 + 1.07\frac{P_s + P_b}{\epsilon}, \tag{18}$$

$$\alpha_4 \equiv 1 + \frac{3A_1 + 3B_2}{B_1}\frac{P_s + P_b}{\epsilon} = 1 + 2.0\frac{P_s + P_b}{\epsilon}. \tag{19}$$

It can be seen from Eq. (8) that the momentum and buoyancy fluxes go to zero if $S_H \rightarrow 0$. It follows from Eq. (15) that this occurs when $R_f \rightarrow \alpha_1/\alpha_2$. This "critical" Richardson number decreases when $(P_s + P_b)/\epsilon$ grows, and it goes to zero when $(P_s + P_b)/\epsilon \rightarrow 3$ as seen from (16)–(17).

In the so-called "boundary layer approximation," where the time derivative and turbulence transport terms in (4) are neglected, $(P_s + P_b)/\epsilon = 1$. The coefficients that then result from Eqs. (16)–(19) will give a value of the critical flux

Richardson number $R_f = \alpha_1/\alpha_2 = 0.19$. The critical *gradient* Richardson number is quite close to the critical R_f and is given by $\mathrm{Ri}_c = \sigma(R_{f*})R_f = 0.17$. Note that the value of the critical gradient Richardson number at a given time will depend sensitively on the nature of the turbulent mixing at that time—in particular, on the relative values of $P_s + P_b$ and ϵ. We will see in the coming discussion that the ratio $(P_s + P_b)/\epsilon$ in our simulations varies from being quite close to 1 to as low as 0.6, with a corresponding impact on the flux Richardson number implied by Eqs. (16)–(17).

Finally, in order to determine the macroscale l, Mellor and Yamada (1982) used an empirical equation that is related to the integral of the two-point correlation functions

$$\frac{\partial q^2 l}{\partial t} = \frac{\partial}{\partial z}\left(lqS_q\frac{\partial q^2 l}{\partial z}\right) + E_1 q l^2 S_H\left[\sigma\left(\frac{\partial \mathbf{V}}{\partial z}\right)^2 - N^2\right] - \frac{q^3}{B_1}\left[1 + E_2\left(\frac{l}{\kappa z}\right)^2\right], \tag{20}$$

where $(S_q, E_1, E_2) = (0.2, 1.8, 1.33)$ and $\kappa = 0.4$ is the von Kármán constant. Equation (20) behaves correctly in the case of grid-generated, decaying turbulence and seems to provide a reasonable length scale in the case of neutral or stratified boundary layers, the latter of which is the subject of this study.

As one proceeds downward from the shear-driven, active turbulence region to the stratification-dominated region below, the present model invariably yields $q \rightarrow 0$ while $l \rightarrow$ constant, and therefore $G_H \rightarrow \infty$ at the lower edge of the turbulent boundary layer. However, experimental and observational studies of shear-free and grid-generated turbulent flows developing in a stably stratified environment generally indicate that G_H is limited by a value smaller than unity (for a review, see Hopfinger 1987). Dickey and Mellor (1980) in their experiments on decaying turbulence in stably stratified fluids found $G_H \approx 0.36$ at the late stages of the decay. Andre et al. (1978), Hassid and Galperin (1983), and Galperin et al. (1988) used the constraint

$$G_H \leqslant 0.28 \tag{21}$$

in their simulations of turbulent entrainment into a stably stratified environment. Note that this constraint also implies $\epsilon \propto N$ in stably stratified flows in agreement with recent estimations of ϵ from direct measurements of small-scale shear in the upper ocean (Gargett and Osborn 1981; Leuck et al. 1983). In practice, the limitation is imposed as a restriction on l, where q and N are determined prognostically and l is then determined according to Eq. (21) (Galperin et al. 1989). We shall see below that the limitation (21) results in exponential decay of turbulence energy, as observed by Smyth et al. (1996).

b. Initial and boundary conditions

The initial velocity $\mathbf{V}$ and turbulent energy E are zero, and vertical profiles of temperature and salinity are chosen to provide a constant buoyancy frequency N_0. The boundary conditions for (1)–(4), (20) at the sea surface, $z = 0$, are

$$\rho_0 lq\sigma S_H\frac{\partial \mathbf{V}}{\partial z} = (\tau_x, \tau_y), \qquad \rho_0 lqS_H\left(\frac{\partial \Theta}{\partial z}, \frac{\partial S}{\partial z}\right) = 0,$$
$$\rho_0 q^2 = B_1^{2/3}\tau, \qquad q^2 l = 0, \tag{22}$$

where (τ_x, τ_y) is the surface wind stress vector, and τ is the magnitude of that vector. In this study, the heat flux and surface freshwater mass flux are taken to be zero.

At the lower boundary, the momentum and buoyancy fluxes, turbulence energy, and macroscale tend to zero;

$$q^2 = q^2 l = 0. \qquad (23)$$

The lower boundary conditions could be applied at any depth below the maximum depth of penetration of turbulence; we choose to apply them at $z = 200$ m. Two types of wind stress evolution were explored: a steplike, impulsively applied constant wind stress acting with a squall duration time t_s:

$$\tau_x = \rho_0 u^2_*, \qquad 0 < t < t_s, \qquad (24)$$

where u_* is the frictional velocity; and a ramplike wind stress that increases linearly with time up to a peak value $2\rho_0 u^2_*$ and then decreases down to zero,

$$\tau_x = 4\rho_0 u^2_* \frac{t}{t_s}, \qquad 0 < t < \frac{t_s}{2};$$

$$\tau_x = 4\rho_0 u^2_* \left(1 - \frac{t}{t_s}\right), \qquad \frac{t_s}{2} < t < t_s. \qquad (25)$$

The set of equations (1)–(4) and (20) were integrated forward in time, utilizing various values for u_*, N_0, and t_s and the two types of wind stress profiles, (24) and (25).

c. Integral budgets and bulk models

The vertically integrated momentum is defined by the surface wind stress from Eq. (1),

$$\mathcal{V}(t) \equiv \int_0^h V_x \, dz = \frac{1}{\rho_0} \int_0^t \tau_x \, dt', \qquad (26)$$

where h is the depth of penetration of the mixing. Equation (26) assumes that the Coriolis force can be neglected for typical squall durations on the order of one hour, when $ft_s \ll 1$. Thus, the total momentum input by the wind,

$$\mathcal{V}_s \equiv \mathcal{V}(t_s) = u^2_* t_s, \qquad (27)$$

will be the same for both steplike (24) and ramplike (25) cases.

The vertically integrated turbulence energy budget from Eq. (4) can be written in the form

$$\frac{d\mathrm{TE}}{dt} = F_0 + \mathrm{SP} + \mathrm{BP} - \mathrm{DIS}, \qquad (28)$$

where the 0 subscript denotes values at the sea surface;

$$\mathrm{TE} \equiv \int_0^h E \, dz, \qquad \mathrm{DIS} \equiv \int_0^h \frac{q^3}{B_1 l} \, dz, \qquad (29)$$

while total shear production

$$\mathrm{SP} \equiv \int_0^h P_s \, dz = \mathbf{V}_0 \langle w\mathbf{v} \rangle_0 - \frac{d\mathrm{KE}}{dt} \qquad (30)$$

and buoyancy flux

$$\mathrm{BP} \equiv \int_0^h P_b \, dz = -\frac{d\mathrm{PE}}{dt}, \qquad (31)$$

are expressed through the time evolution of mean kinetic energy, KE, and potential energy, PE, defined as

$$\mathrm{KE} = \int_0^h \frac{\mathbf{V}^2}{2} \, dz, \qquad \mathrm{PE} = \int_0^h \frac{N^2 z^2}{2} \, dz. \qquad (32)$$

Thus, the rate of change of the total energy, KE + PE + TE, can be shown to be the sum of the surface wind stress work $\mathbf{V}_0 \langle w\mathbf{v} \rangle_0$ and the surface turbulent flux F_0, less the integrated dissipation rate, DIS.

In the bulk model of Pollard et al. (1973), the eddy coefficients in the mixed layer are assumed so large that the velocity and density profiles are 1: $V_x = \mathcal{V}/h$ and $N = \Delta b \delta(z - h)$, where $\Delta b = 0.5 N^2_0 h$ is the buoyancy jump at the base of mixed layer. In this case

$$\mathrm{KE} = \frac{\mathcal{V}^2}{2h}, \qquad \mathrm{PE} = \frac{N_0^2 h^3}{12}, \qquad (33)$$

and the shear production is expressed from Eq. (30), using the integrated momentum balance (26), in the form

$$\mathrm{SP} = \frac{\tau \mathcal{V}}{\rho_0 h} - \frac{d}{dt}\frac{\mathcal{V}^2}{2h} = \frac{\mathcal{V}^2}{2h^2}\frac{dh}{dt}. \qquad (34)$$

Thus, the turbulence energy budget (28) becomes

$$\left(\frac{N_0^2 h^2}{4} - \frac{\mathcal{V}^2}{2h^2}\right)\frac{dh}{dt} = F_0 - \mathrm{DIS} - \frac{d\mathrm{TE}}{dt}. \qquad (35)$$

Assuming that the rhs of (35) is equal to C_DSP, where C_D is a proportionality constant, Pollard et al. (1973) transformed (35) into

$$\left(\frac{N_0^2 h^2}{4} - (1 - C_D)\frac{\mathcal{V}^2}{2h^2}\right)\frac{dh}{dt} = 0. \qquad (36)$$

Thus, in their model, the mixed layer depth is determined by the initial buoyancy frequency and the total momentum input by the wind

$$h = C_B h_B(t), \qquad h_B \equiv \left(\frac{\mathcal{V}(t)}{N_0}\right)^{1/2}, \qquad (37)$$

where the coefficient $C_B = [2(1 - C_D)]^{1/4} \approx 1$. This bulk mixing depth $h_B(t)$ will be compared with the depth of penetration of turbulence calculated from the MY2.5 model.

3. Results and discussion

a. Dimensionless formulation

When the initial turbulent energy is zero, the depth of penetration of turbulence, $h(t)$, remains finite in the MY2.5 model: $E = 0$ for $z > h$ (the turbulent layer $z < h$ will be referred to as the “mixing” layer in all subsequent discussion). Thus, for constant initial buoyancy frequency, all dynamical quantities can be represented by dimensionless functions of $N_0 t$ and z/h after normalizing by specially chosen scales,

$$\frac{V_x}{V_*} = U\left(N_0 t, \frac{z}{h}\right), \qquad \frac{q^2}{E_*} = Q\left(N_0 t, \frac{z}{h}\right),$$

$$\frac{l}{h} = L\left(N_0 t, \frac{z}{h}\right), \qquad \frac{N}{N_0} = G\left(N_0 t, \frac{z}{h}\right). \qquad (38)$$

Here, the mean velocity scale is defined by the vertically integrated momentum

$$V_* = \frac{\mathcal{V}}{h}, \qquad (39)$$

the turbulence energy scale is related to the bulk dissipation rate in Eq. (29)

$$E_* = (\mathrm{DIS})^{2/3}, \qquad (40)$$

and it is assumed that the macroscale can be normalized by the mixing depth h. The scales, which may depend on time, are chosen in such a way that the dimensionless functions U, Q, L, G are all of order one.

Figure 1 shows the results of four experiments in which the wind stress was held constant for a dimensionless time of $N_0 t = 288$ and then removed. For the remainder of this paper, the period during the wind forcing will be referred to as the "squall" regime and the subsequent period with no wind will be referred to as the "decay" regime. The four experiments consist of the possible combinations of two different values of both N_0 and u_*. The vertical resolution Δz was 12.5 cm for all experiments. The excellent agreement in the dimensionless velocity and buoyancy profiles among the various experiments demonstrates that the model is robust and that the solution responds to variations in the external parameters according to (38)–(40).

For any combination of u_* and N_0, given the same dimensionless squall duration $N_0 t_s$, and squall type, the results in dimensionless representation (38) should be identical, as was the case for the first suite of experiments. From here on, our experiments will consist of variations of only the squall duration and type.

b. Squall stage

Turning our attention to the details of the model evolution, two different physical regimes can be detected during the squall period. We will refer to these regimes as the transition stage and the asymptotic stage, respectively. At the very initial stage of squall forcing (when $N_0 t \ll 1$), the effect of stratification is negligible and h grows linearly with time, the velocity scale stays proportional to u_*, and the turbulent energy scale is proportional to u_*^2, as shown by Mellor and Strub (1980).

As $N_0 t$ grows, we see a transition period toward an asymptotic stage characterized by self-similar vertical profiles for $N_0 t \to \infty$

$$V_x = V_* U_a\left(\frac{z}{h}\right), \qquad q^2 = E_* Q_a\left(\frac{z}{h}\right),$$

$$l = h L_a\left(\frac{z}{h}\right), \qquad N = N_0 G_a\left(\frac{z}{h}\right). \qquad (41)$$

As shown by Kundu (1981) and Sutyrin (1984), the assumption of self-similarity implies that the turbulence penetration depth is proportional to the bulk mixing depth:

where C_a is a constant. The mean velocity scale grows as

$$V_* = \frac{u_*}{C_a}(tN_0)^{1/2} \qquad (43)$$

because the integrated momentum $\mathcal{V} = u^2_* t$, and the turbulence energy scale grows as

$$E_* = C_E u^2_* (tN_0)^{1/3}, \qquad (44)$$

as follows from Eq. (28), where the bulk dissipation is expected to be proportional to the surface wind work.

The transition of the model solution from initial linear growth with time to the asymptotic power law (42) is demonstrated in Fig. 2a where the ratio h/h_B indicates that $C_a \approx 1$. The ratio $E_*/u^2_*(tN_0)^{1/3}$ decreases during the transition period and C_E approaches 1 (Fig. 2b). An approach to the self-similar asymptotic state is also seen in the dimensionless profiles of velocity V/V_* and buoyancy frequency N/N_0, which are nearly the same for $N_0 t = 144$ and $N_0 t = 288$ (Fig. 3).

From these simulations we see that the mixed layer can be divided into two sublayers where different physical processes dominate. This two-layer structure is typical of a wind-deepening mixed layer. In the upper sublayer, the macroscale grows almost linearly with depth and reaches a maximum at $z = h_1$ (Fig. 4a). During the squall $h_1 \approx 0.8\,h$. After the transtion stage, the turbulence energy also displays a maximum in its vertical profile, at nearly the same depth as that for l (Fig. 4b). In the lower sublayer, both the macroscale and turbulence energy rapidly decrease with depth, going to zero just below the mixing layer. In the upper sublayer, the Richardson number is well below the critical value, indicating strong mixing due to turbulent fluxes, and N becomes smaller than N_0. In the smaller, lower sublayer, however, the buoyancy frequency is larger than N_0 and the Richardson number approaches a value $\mathrm{Ri}_c = 0.17$ (Fig. 5). This is close to the critical value mentioned in section 2 for nearly stationary mixing, that is, when $P_s + P_b \approx \epsilon$ and $dE/dt \approx 0$. The simulated values of these parameters reveal us to be in just such a regime in the lower sublayer.

c. Decay stage

During the decay phase, there is a transition period when the large vertical shear in the surface layer disappears (Fig. 1b), and subsequently, there is almost no change in either the velocity or buoyancy frequency profiles. After this transition period, the turbulence energy decays substantially while the Richardson number tends toward a constant in the mixing layer, which, it will be shown, has important implications for the rest of the analysis.

The present simulations provide a useful context to examine the conclusions in the observational work by Smyth et al. (1996). Figure 6 shows the model evolution of the various terms in the turbulence energy balance (4) at depths $z = 0.2h$ and $z = 0.8h$ during the decay phase, normalized by the TKE dissipation rate ϵ. Several features deserve emphasis. First one notes that, after the transition phase immediately following the removal of the wind, all terms, P_s/ϵ, P_b/ϵ, dF/dz and $(dE/dt)/\epsilon$, approach constant values. Moreover, the values of these terms are nearly the same in the upper and lower parts of mixing layer, so that $(P_s + P_b)/\epsilon \approx 0.6 < 1$ during the asymptotic decay stage. Thus, the Richardson number can reach a higher value of $\mathrm{Ri}_c \approx 0.3$, as follows from Eqs. (16)–(17).

The other point to note about the decay is that the shear production and buoyancy production terms represent a significant fraction of the overall TKE balance (Fig. 6). Most notably, the magnitude of the shear production source term is nearly 80% of the dissipation term even in the absence of wind forcing. This, too, supports the observational analysis of Smyth et al. (1996), who hypothesized that such a source term should be present to explain the observed rate of TKE decay.

After the transition period, the decay rate, characterized by $E^{-1}dE/dt \approx 0.04N_0$, does not vary essentially, indicating that the turbulence decay is nearly exponential, as found in the observations by Brainerd and Gregg (1993) and Smyth et al. (1996). This is, perhaps, no surprise given the nature of the model formulation, as will be described in what follows. With the dissipation term $\epsilon \propto q^3/l$, it can readily be shown that $\epsilon \propto q^2$ if the macroscale follows the Ozmidov scale L_O:

$$l \simeq C_l L_O, \qquad L_O = \left(\frac{\epsilon}{N^3}\right)^{1/2}, \qquad (45)$$

where C_l is a proportionality constant. Let us assume for the moment that this is the case. Since, for all but the initial portion of the decay phase, all terms in Eq. (4) are proportional to ϵ, the decay of all terms will be exponential. This argument ignores the time evolution of N, but our results indicate the N profile is remarkably static during the decay phase.

In our experiments, l was limited by the condition (21). When the equality in this expression holds, as was the case for most of the mixed layer during the asymptotic decay phase, it can easily be seen that $l \approx 4L_O$. The exponential decay we observe, then, is a logical consequence of the restriction (21), provided that l becomes large enough (or q/N becomes small enough) that the restriction comes into play. That this is in fact the case is demonstrated by Fig. 7, which shows the vertical profile of G_H for several different times. One sees G_H is at its limiting value over an increasingly large fraction of the mixing layer as time progresses. It should perhaps be noted that this limitation does not significantly affect any of the other conclusions of this work. In particular, the universality during the decay stage discussed in the following section is observed regardless of whether or not a limitation on G_H is imposed.

d. Universality of the final stage

In this section, we demonstrate that the model solutions for a variety of forcing scenarios can be characterized by a simple universal form. Assuming the gradient Richardson number is nearly constant in the asymptotic decay regime, one can rearrange the definition of this number and integrate vertically to find

$$\mathcal{V}_s = \mathrm{Ri}^{-1/2} \int_0^h Nz\, dz = N_0 h^2 / C_R^2,$$

$$C_R = \mathrm{Ri}^{1/4} \left(\int_0^1 \frac{N}{N_0} \eta\, d\eta \right)^{-1/2}, \qquad (46)$$

where $\eta = z/h$ is normalized depth. Thus the mixed layer depth should be proportional to the bulk mixed layer depth (37)

$$h = C_R \left(\frac{\mathcal{V}_s}{N_0} \right)^{1/2}. \qquad (47)$$

The coefficient C_R depends on the vertical profile of the buoyancy frequency and the value of Ri in the asymptotic decay regime.

Equation (47) provides a simple relationship between the final mixed layer depth and the total momentum input $\mathcal{V}_s$, provided that the coefficient C_R is not highly sensitive to the forcing history. To explore this question, we performed a series of experiments in which the wind profile and squall duration were varied. The first of these consisted of a comparison between cases in which the wind forcing was either ramplike or steplike, as described earlier. For a given squall duration, t_s, the total momentum input was the same for the two cases. The results demonstrate that, though the evolution of the model state was indicative of the steplike or ramplike nature of the forcing during the squall period, the asymptotic decay state was nearly identical for the two different forcing histories. Figure 8 shows a comparison of h for the two cases when $N_0 t_s = 72$ ($t_s = 2$ h for the N_0 used here). One can see discrepencies reflective of the fact that the wind was ramped up and down in one case and held constant in the other for times prior to and immediately following $N_0 t_s$. Of particular note is the transition regime that immediately follows the squall. Up to $N_0 t = 100$, shear at the base of the mixed layer is still producing significant additional deepening of h. Discrepancies between the two forcing profiles are still apparent in this period. After this point, when the terms in the TKE balance achieve their constant relative values and the deepening of h ceases, the two forcing cases are nearly indistinguishable.

The dependence of the final stage on squall duration was also explored for both squall types. Experiments were performed with squall durations of $N_0 t_s = 18$, 36, 72, and 144. The value of C_R, defined by Eq. (47), is plotted versus $N_0 t_s$ for both

wind forcing cases in Fig. 9. It can readily be seen that C_R is essentially a constant ~ 1.07, regardless of squall duration or forcing type. This apparent universality of C_R, and hence the dependence h on only the initial stratification and total momentum input, can be shown to be a logical consequence of Eq. (46) provided that two things are true: the gradient Richardson number is a constant nearly independent of depth, forcing profile, or forcing duration and the final normalized N profile has a universal form. Figure 10 shows profiles of Richardson number and N/N_0 at the final stage for two different squall durations and the two forcing profiles. It is apparent that the present model solution meets both of the conditions for universality of C_R. As is evident from Eqs (16)–(17), the tendency toward a constant Richardson number is a consequence of the MY2.5 model formulation. However, the universality of the N profile is not obvious and remains a topic for further inquiry.

4. Summary

A one-dimensional turbulence closure model was used to explore tropical ocean mixed layer turbulent response to squall-like forcing and the subsequent decay of that turbulence. Experiments were performed in which an initially quiescent, uniformly stratified ocean was forced with squalls of various durations and wind evolution profiles. Several physical regimes of turbulent mixing and decay during and after wind forcing were described.

While the wind forcing was being applied, we observed a tendency toward a regime in which vertical profiles of various quantities were self-similar. The mixing depth h approached the bulk value h_B and the turbulent energy scale E_* approached $u^2_*(tN_0)^{1/3}$. Proceeding down the water column, the mixed layer tended to behave as two sublayers, separated by maxima in l and q^2, where the stratification switches from being less than N_0 to being greater than N_0 and the Richardson number changes from being supercritical to near critical.

After the wind was shut off, the turbulent kinetic energy was shown to decay nearly exponentially with time and TKE source terms such as shear production were demonstrated to play an important role. The decay period was seen to be characterized by universal forms for the velocity and density profiles and the Richardson number was observed to be nearly independent of depth and forcing history. This enabled a description of the depth of maximum penetration of turbulence as a function of only the total time-integrated momentum input and the initial density profile in a manner analogous to bulk models.

Acknowledgments

This research was supported by the National Science Foundation through Grant ATM 9319462.

REFERENCES

Andre, J. C., and P. Lacarrere, 1985: Mean and turbulent structure of the oceanic surface layer as determined from one-dimensional third-order simulations. *J. Phys. Oceanogr.*, **15,** 121–132.. Find this article online

— ,G. De Moor, P. Lacarrere, G. Therry, and R. du Vachat, 1978:Modeling the 24-hour evolution of the mean and turbulent structures of the planetary boundary layer. *J. Atmos. Sci.*, **35,** 1861–1883.. Find this article online

Batchelor, G. K., and A. A. Townsend, 1948: Decay of isotropic turbulence in the initial period. *Proc. Roy. Soc. London, Ser. A.*, **193,** 539–558..

Brainerd, K. E., and M. C. Gregg, 1993: Diurnal restratification and turbulence in the oceanic surface mixed layer. Part 2: Modeling. *J. Geophys. Res.*, **98,** 22 657–22 664..

Caldwell, D. R., 1983: Oceanic turbulence: Big bangs or continuous creation? *J. Geophys. Res.*, **88,** 7543–7550..

Chen, D., L. M. Rothstein, and A. J. Basalacchi, 1994: A hybrid vertical mixing scheme and its applications to tropical ocean models. *J. Phys. Oceanogr.*, **24,** 2156–2179.. Find this article online

Crawford, W. R., 1986: A comparison of length scale and decay times of turbulence in stably stratified fluids. *J. Phys. Oceanogr.*, **16,** 1847–1854.. Find this article online

D'Asaro, E. A., 1985: Ocean Storms—A three-dimensional, severe storm, air/sea interaction experiment: Overview and core program manuscript. Applied Physics Laboratory, University of Washington, 39 pp..

Dickey, T. D., and G. L. Mellor, 1980: Decaying turbulence in neutral and stratified fluids. *J. Fluid Mech.*, **99,** 13–31..

Dillon, T. M., 1982: Sampling turbulent dissipation. *J. Geophys. Res.*, **87,** 541–549..

Galperin, B., L. H. Kantha, S. Hassid, and A. Rosati, 1988: A quasi-equilibrium turbulent energy model for geophysical flows. *J. Atmos. Sci.*, **45,** 155–165.. Find this article online

— ,A. Rosati, L. H. Kantha, and G. L. Mellor, 1989: Modeling rotating stratified turbulent flows with application to oceanic mixed layers. *J. Phys. Oceanogr.*, **19,** 901–916.. Find this article online

Gargett, A. E., and T. R. Osborn, 1981: Small-scale shear measurements during the Fine and Microstructure Experiment (FAME). *J. Geophys. Res.*, **86,** 1929–1944..

Gibson, C. H., 1982: Alternative interpretation for microstructure patches in the thermocline. *J. Phys. Oceanogr.*, **12,** 374–383.. Find this article online

Gregg, M. C., 1987: Diapycnal mixing in the thermocline: A review. *J. Geophys. Res.*, **92,** 5249–5286..

Hassid, S., and B. Galperin, 1983: A turbulent energy model for geophysical flows. *Bound.-Layer Meteor.*, **26,** 397–412..

Hopfinger, E. J., 1987: Turbulence in stratified fluids: A review. *J. Geophys. Res.*, **92,** 5287–5303..

Klein, P., and M. Coantic, 1981: A numerical study of turbulent process in the marine upper layers. *J. Phys. Oceanogr.*, **11,** 849–863.. Find this article online

Kraus, E. B., 1988: Merits and defects of different approaches to mixed layer modeling. *Small-Scale Turbulence and Mixing in the Ocean,* J. C. J. Nihoul and B. M. Jamart, Eds., Elsevier, 37–50..

— ,and J. S. Turner, 1967: A one-dimensional model of the seasonal thermocline, Part II. *Tellus,* **19,** 98–105..

Kundu, P. J., 1980: A numerical investigation of mixed layer dynamics. *J. Phys. Oceanogr.*, **10,** 220–236.. Find this article online

— ,1981: Self-similarity in stress-driven entrainment experiments. *J. Geophys. Res.*, **86**(C), 1979–1988..

Leuck, R., W. R. Crawford, and T. R. Osborn, 1983: Turbulent dissipation over the continental slope off Vancouver Island. *J. Phys. Oceanogr.*, **13,** 1809–1818.. Find this article online

Martin, P., 1985: Simulation of the mixed layer at OWS November and Papa with several models. *J. Geophys. Res.*, **90,** 903–915..

Mellor, G. L., and P. A. Durbin, 1975: The structure and dynamics of the ocean surface mixed layer. *J. Phys. Oceanogr.*, **5,** 718–728.. Find this article online

— ,and P. T. Strub, 1980: Similarity solutions for the stratified turbulent Rayleigh problem. *J. Phys. Oceanogr.*, **10,** 455–460.. Find this article online

— ,and T. Yamada, 1982: Development of a turbulent closure model for geophysical fluid problems. *Rev. Geophys. Space Phys.*, **20,** 851–875..

Moum, J. N., 1996: Energy-containing scales of stratified turbulence. *J. Geophys. Res.*, **101,** 12 057–12 069..

Munk, W. H., and E. R. Anderson, 1948: A note on the theory of the thermocline. *J. Mar. Res.*, **7,** 276–295..

Niiler, P. P., 1975: Deepening of the wind-mixed layer. *J. Mar. Res.*, **33,** 405–422..

— ,and E. B. Kraus, 1977: One-dimensional models of the upper ocean. *Modelling and Prediction of the Upper Layers of the Ocean,* E. B. Kraus, Ed., Pergamon Press, 143–172..

Pollard, R. T., P. B. Rhines, and R. O. R. Y. Thompson, 1973: The deepening of the wind mixed layer. *J. Geophys. Fluid. Dyn.*, **3,** 381–404..

Price, J. F., R. A. Weller, and R. Pinkel, 1986: Diurnal cycling: observations and models of the upper ocean response to diurnal heating, cooling, and wind mixing. *J. Geophys. Res.*, **91,** 8411–8427..

Smyth, W. D., P. O. Zavialov, and J. N. Moum, 1996: Decay of turbulence in the upper ocean following sudden isolation from surface forcing. *J. Phys. Oceanogr.*, **27,** 810–822.. Find this article online

Sutyrin, G. G., 1984: Turbulent mixing in a stratified shear layer. *Dokl. Akad. Nauk SSSR, Earth Sciences,* **277,** 32–36..

Webster, P. J., and R. Lukas, 1992: TOGA COARE: The Coupled Ocean–Atmosphere Response Experiment. *Bull. Amer. Meteor. Soc.,* **73,** 1377–1416.. Find this article online

---

Figures

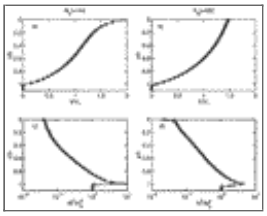

Click on thumbnail for full-sized image.

Fig. 1. Normalized velocity and buoyancy frequency profiles during and after the squall. The wind was removed at $N_0 t = 288$. Each plot shows the results of four experiments. The solid line is for $N_0 = 0.01\ s^{-1}$ and $u* = 0.01\ m\ s^{-1}$, the dashed line is for $N_0 = 0.01\ s^{-1}$ and $u* = 0.02\ m\ s^{-1}$, the open circles are for $N_0 = 0.005\ s^{-1}$ and $u* = 0.01\ m\ s^{-1}$, and the pluses are for $N_0 = 0.005\ s^{-1}$ and $u* = 0.02\ m\ s^{-1}$.

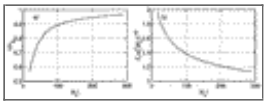

Click on thumbnail for full-sized image.

Fig. 2. Evolution of the scales for (a) mixing depth and (b) turbulent kinetic energy during the squall.

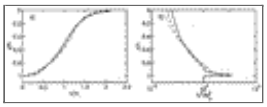

Click on thumbnail for full-sized image.

Fig. 3. Evolution of (a) normalized velocity and (b) buoyancy frequency profiles. The solid line is for $N_0 t = 72$, the dashed line is for $N_0 t = 144$, and the dotted line is for $N_0 t = 288$. In this experiment, $N_0 = 0.01\ s^{-1}$ and $u* = 0.02\ m\ s^{-1}$.

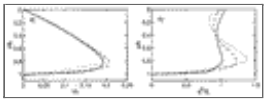

Click on thumbnail for full-sized image.

Fig. 4. (a) Turbulence macroscale and (b) turbulent energy profiles for times $N_0 t = 72$ (solid), $N_0 t = 144$ (dashed), and $N_0 t = 288$ (dotted) during the squall.

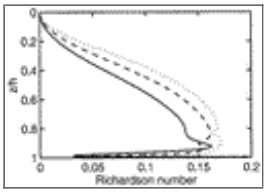

Click on thumbnail for full-sized image.

Fig. 5. Ri profiles for times $N_0 t = 72$ (solid), $N_0 t = 144$ (dashed), and $N_0 t = 288$ (dotted) during the squall.

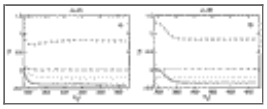

Click on thumbnail for full-sized image.

Fig. 6. Evolution of TKE terms at (a) 0.2h and (b) 0.8h. The plots show the shear production term (dashed), the buoyancy production/loss term (dotted), the vertical turbulent energy flux term (dot-dash), and dE/dt (solid), all normalized by the TKE dissipation rate ϵ.

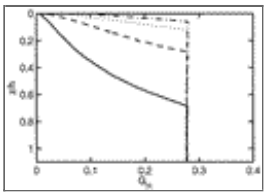

Click on thumbnail for full-sized image.

Fig. 7. G_H profiles for times N_0t = 324 (solid), N_0t = 360 (dashed), N_0t = 396 (dotted), and N_0t = 432 (dot–dash) after the squall. The wind forcing ended at N_0t = 288.

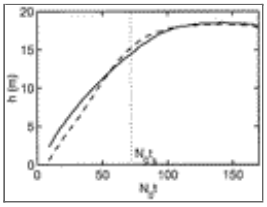

Click on thumbnail for full-sized image.

Fig. 8. Turbulence penetration depth evolution for stepped (dashed) and ramped (solid) wind cases when N_0t_s = 72.

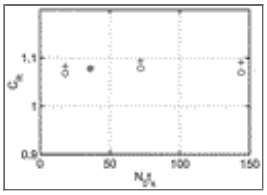

Click on thumbnail for full-sized image.

Fig. 9. C_R for four different squall shut-off times, t_s. Ramped wind results are indicated with circles, stepped wind results with pluses.

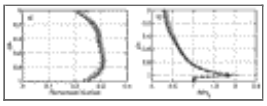

Click on thumbnail for full-sized image.

Fig. 10. Profiles of (a) Ri and (b) N/N_0 at $N_0t = N_0t_s + 72$. The results for four experiments are shown in each plot. N_0t_s = 36 for the ramped (solid) and stepped (circles) cases, and N_0t_s = 72 for the ramped (dashed) and stepped (pluses) cases.

Corresponding author address: Dr. Raymond A. Richardson, Graduate School of Oceanography, University of Rhode Island, Narragansett, RI 02882.

E-mail: rayr@auke.gso.uri.edu

top